

¹⁷J. Banaigs, J. Berger, C. Bonnel, J. Duflo, L. Goldzahl, F. Plouin, W. F. Baker, P. J. Carlson, V. Chabaud, and A. Lundby, Nucl. Phys. **B9**, 640 (1969).

¹⁸W. F. Baker, K. Berkelman, P. J. Carlson, G. P. Fisher, P. Fleury, D. Hartill, R. Kalbach, A. Lundby, S. Mikhin, R. Nierhaus, K. P. Pretzl, and J. Woulds, Phys. Letters **28B**, 291 (1968).

¹⁹V. Chabaud, A. Eide, P. Lehmann, A. Lundby, S. Mikhin, J. Myrheim, C. Baglin, P. Briandet, P. Fleury, P. Carlson, E. Johansson, M. Davier, V. Gracco, R. Morand, and D. Treille, Phys. Letters **38B**, 445 (1972).

²⁰We have used the same form for $\gamma(u)$ as Barger (Ref. 11).

²¹H. Harari, Phys. Rev. Letters **22**, 562 (1969); J. L. Rosner, *ibid.* **22**, 689 (1969).

²²Duality predictions are not expected to hold *exactly*. Several reactions predicted to have purely real amplitudes are observed to have nonzero polarizations, indicating some breaking of these predictions. See, for example, R. D. Field and J. D. Jackson, Phys. Rev. **D4**, 693 (1971).

²³For a compilation of various determinations of the $KN\Lambda$ and $KN\Sigma$ couplings see Ref. 14.

PHYSICAL REVIEW D

VOLUME 7, NUMBER 1

1 JANUARY 1973

Analysis of $K^-p \rightarrow \Lambda\pi^+\pi^-$ in the Region of the $\Lambda(1520)$

Terry S. Mast, Margaret Alston-Garnjost, Roger O. Bangerter, Angela Barbaro-Galtieri, Frank T. Solmitz, and Robert D. Tripp

Lawrence Berkeley Laboratory, University of California, Berkeley, California 94720

(Received 3 May 1972)

The rate for the decay $\Lambda(1520) \rightarrow \Sigma(1385)\pi$ has been measured in a study of the reaction sequence $K^-p \rightarrow \Lambda(1520) \rightarrow \Sigma(1385)\pi \rightarrow \Lambda\pi^+\pi^-$. A sample of 9200 events of the type $K^-p \rightarrow \Lambda\pi^+\pi^-$ has been obtained in the Berkeley 25-in. hydrogen bubble chamber. The incident momenta range from 300 to 470 MeV/c. An energy-independent partial-wave analysis was performed using an isobar model. The model included a coherent mixture of six partial waves to describe all mass distributions, angular distributions, and the polarization of the Λ . The $\Sigma(1385)\pi$ decay mode was found to dominate the $\Lambda\pi^+\pi^-$ decay of the $\Lambda(1520)$, in disagreement with the results of a production reaction study of the same decay. The width for the decay was measured to be 1.40 ± 0.26 MeV. Mixing between the $\Lambda(1520)$ and the $\Lambda(1690)$ has been used in the past to describe the $J^P = \frac{3}{2}^-$ baryons as SU(3) singlet and octet. Combining our rate for $\Lambda(1520)$ with a recently measured rate for $\Lambda(1690) \rightarrow \Sigma(1385)\pi$, we calculate the mixing angle $|\theta| = 63^\circ$ to 83° . This is in strong disagreement with the mixing angle derived from the two-body D -wave decays of the singlet and octet of $-25 \pm 6^\circ$. Thus, some modification of the usual SU(3) description of these states needs to be made.

I. INTRODUCTION

Within the framework of SU(3), the known $J^P = \frac{3}{2}^-$ baryons have been treated as a singlet and octet by several authors.^{1,2} The rates for the D -wave decays of the octet disagree with the predictions of SU(3), and the masses of the octet members fail to satisfy the Gell-Mann-Okubo mass relation. These discrepancies have been successfully removed by invoking configuration mixing between the primarily singlet state $\Lambda(1520)$ and the primarily octet state $\Lambda(1690)$. Data now are becoming available on the S -wave decays of these states into members of the $\frac{3}{2}^+$ decuplet and the 0^- meson octet.³⁻⁶ These provide a further test of the SU(3) nature of these baryons. For example, if the $\Lambda(1520)$ were a pure SU(3) singlet, then its decay through an SU(3)-invariant process to $\Sigma(1385)\pi$ would be forbidden. Consistent with the

mixed nature of the $\Lambda(1520)$, however, this decay is observed. The rate for the decay was measured in a production experiment⁵ and a formation experiment,³ and the mixing angles calculated from those rates were consistent with the angle derived from the mass relation and the D -wave decays.^{1,2}

In this experiment, we study the decay in the formation reaction $K^-p \rightarrow \Lambda(1520) \rightarrow \Sigma(1385)\pi$.⁷ An increase in the number of events by a factor of 100 from the experiment⁸ which discovered the $\Lambda(1520)$ allows a very detailed analysis. In Sec. II we describe the experimental procedures, the bias corrections applied to the data. In Sec. III we describe the over-all features of the data. The Dalitz plot is dominated by $\Sigma(1385)$ production. The angular distribution of the Λ indicates dominance of $J^P = \frac{3}{2}^-$ formation. In order to extract the modes and rates for the decay of $\Lambda(1520)$ from

the data, we have performed a partial-wave analysis of the three-particle final state using an isobar model. This analysis is described in Secs. IV and V and yields information about the formation process as well as the decay modes of $\Lambda(1520)$. The rate into $\Sigma(1385)\pi$ disagrees with the result from the previous measurements^{3,5} by more than a factor of 2. In Sec. VI, the result from our experiment is combined with other data on the $\frac{3}{2}^-$ baryons to yield a new mixing angle. This value for the mixing angle strongly disagrees with the value derived from the two-body D -wave decays. The Appendix gives the detailed formulas used in the isobar model.

II. EXPERIMENTAL PROCEDURES

The K^- beam for this experiment was designed and built by Murray and Bangerter, and was operated in conjunction with the Berkeley 25-in. hydrogen bubble chamber. The beam has been fully described elsewhere.⁹

An exposure of 1.3×10^6 pictures was obtained. Typically each picture contained six K^- tracks and two background tracks. The background consisted of pions, muons, and some electrons. Background tracks had close to minimum ionization and were thus easily distinguished from the K^- tracks, which at our momentum has approximately three times minimum ionization.

By movement of the target and by use of a beryllium beam degrader, we were able to obtain K^- momenta between 270 and 470 MeV/c. The data were taken with 20 different beam settings. However, most of the pathlength (Fig. 1) occurs close to 395 MeV/c, the momentum required to form the $\Lambda(1520)$.

The film was scanned for all topologies including those with a Λ decay and two charged pions in the final state. All of the film was scanned once; 38%

was scanned twice; and 7% was scanned three times. All events within a restricted fiducial volume were measured with the Spiral Reader or Franckenstein measuring projectors. The kinematic reconstruction and the fit to reaction hypothesis were performed with the programs TVGP and SQUAW. Events which failed to fit a reaction hypothesis were remeasured until 91% of the total sample of the $\Lambda\pi\pi$ events passed. The remaining failing events were unmeasurable due to the obscuration of a track or the presence of a very short track.

A sample of τ decays of the beam was measured and fitted in order to determine the beam characteristics for each of the 20 beam settings. The mean momentum, the rms spread of the momentum, and a momentum position correlation were established for each setting. The mean momentum from the τ decays was averaged with the measured momentum for each of the $\Lambda\pi\pi$ events prior to the fitting to a reaction hypothesis. The magnetic field in the chamber was 18.7 kG, and the beam tracks were typically measured with an uncertainty of ± 8 to ± 12 MeV/c. After beam averaging and fitting to $K^-p \rightarrow \Lambda\pi^+\pi^-$, the final sample of events had a mean uncertainty of ± 3.6 MeV/c and the distribution shown in Fig. 2.

Only those events which fitted a reaction hypothesis with a confidence level greater than 0.01 were accepted for further analysis; 11 800 such events satisfied the 7-constraint fit to $K^-p \rightarrow \Lambda\pi^+\pi^-$ and 336 events passed the 5-constraint fit to $K^-p \rightarrow \Sigma^0\pi^+\pi^-$. Ten ambiguous events fit both hypotheses. Reinspection showed them to be mismeasured and they were eliminated from the sample.

To ensure sufficient tracklength for a good measurement of the Λ momentum, further restrictions were made on the fiducial volumes for the production and decay vertices. These reduced the sample to 10 296 events. To correct for a scanning loss of short-length Λ 's, all events with a projec-

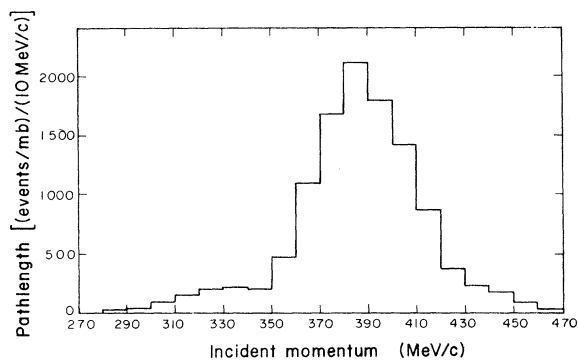


FIG. 1. Pathlength [(events/mb)/(10 MeV/c)] as a function of incident K^- momentum (MeV/c).

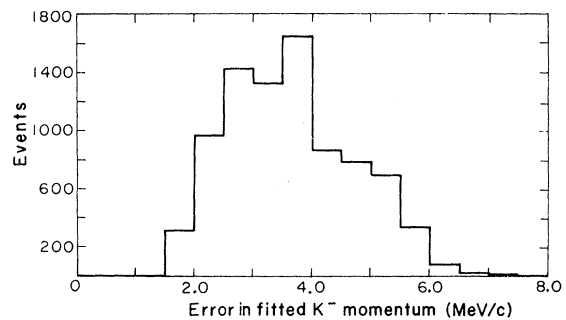


FIG. 2. Histogram of the error in the fitted K^- momentum in MeV/c.

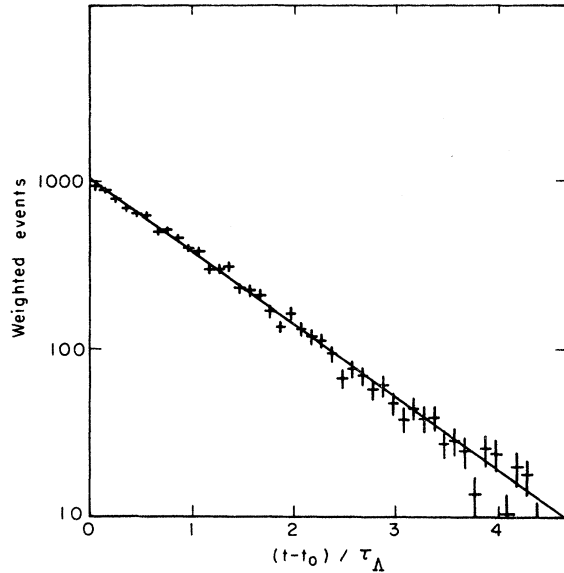


FIG. 3. Λ lifetime distribution. Each event is plotted at $(t-t_0)$ to remove the effect of the cut on short-length Λ 's. The value of t_0 for each event is described in the text. The straight line corresponds to the known Λ lifetime.

ted length less than 2.5 mm were eliminated and the remaining 9412 events were weighted to account for the cut. The weighting also accounted for loss due to escape from the decay vertex fiducial volume. The mean weight was 1.18. Further losses were investigated by looking at the distribution of the decay proton in the Λ rest frame. Anisotropy in this distribution was found coming from the loss of events with short-length protons and events with the Λ decay seen edge on by the scanners. These biases were removed by rejecting events with a proton length less than 3 mm and weighting the remaining events. This reduced the sample to 9227 events with a mean weight of 1.21. A detailed description of the analysis and application of these cuts and weights is given in Ref. 10.

The lifetime distribution of the final sample is shown in Fig. 3. In order to remove the effect of the cut on short-length Λ 's, the events have been plotted as a function of $(t-t_0)$ in units of the known Λ lifetime. For each event, t_0 is given by $2.5 \text{ mm}/\eta c \tau_\Lambda \cos \lambda$, where η is the ratio of the Λ momentum to its mass and λ is the dip angle. The distribution is consistent with the line corresponding to the known lifetime ($\tau_\Lambda = 2.51 \times 10^{-10}$ sec).

The cross section for the reaction was determined from a pathlength based on the τ decays of the beam. The analysis of these τ 's has been described in a previous publication.¹¹ The numbers of both τ 's and $\Lambda \pi \pi$ events were corrected for unobserved decay modes and for scanning effi-

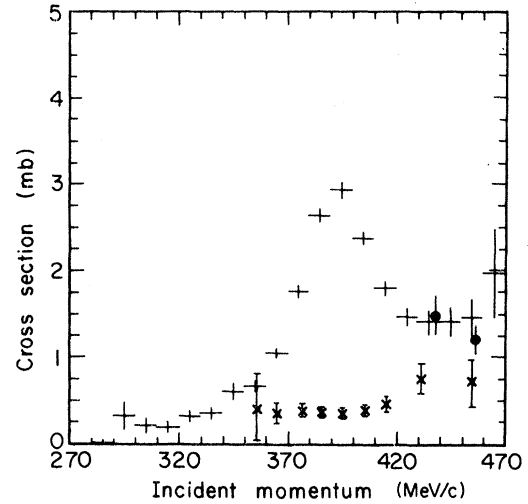


FIG. 4. The partial cross section for $K^-p \rightarrow \Lambda \pi^+ \pi^-$ in millibarns as a function of incident momentum (MeV/c). The two dotted points are results from Ref. 12. The crossed points are the predictions for the background from the fit described in the text.

ciencies.

The scanning efficiencies were determined from the multiple scans using an extension of the method developed by Derenzo and Hildebrand.¹² The analysis accounts for the differing visibility of events by parametrizing a visibility function $f(v)$; $f(v)$ is the fraction of the sample seen with an efficiency v , where v varies from 0.0 to 1.0. The extension

TABLE I. Partial cross sections for $K^-p \rightarrow \Lambda \pi^+ \pi^-$ with statistical errors only.

Momentum (MeV/c)	Cross section σ (mb)	Weighted $\Lambda \pi^+ \pi^-$ events
295	0.32 ± 0.17	7
305	0.21 ± 0.09	11
315	0.19 ± 0.07	17
325	0.32 ± 0.07	39
335	0.35 ± 0.07	47
345	0.61 ± 0.10	77
355	0.67 ± 0.06	195
365	1.05 ± 0.06	717
375	1.77 ± 0.06	1863
385	2.64 ± 0.08	3491
395	2.93 ± 0.09	3298
405	2.33 ± 0.09	2114
415	1.80 ± 0.09	982
425	1.46 ± 0.11	338
435	1.41 ± 0.15	200
445	1.41 ± 0.17	151
455	1.45 ± 0.23	84
465	1.97 ± 0.52	30

used for this experiment defines a different visibility (v_1 , v_2 , and v_3) for each of the three scans. The events found on each of the scans are fitted to determine the parameters of the function $f(v_1, v_2, v_3)$, which is then used to calculate the efficiencies. Details of this analysis can be found in Ref. 13. The over-all scanning efficiency was 0.96.

The beam-averaging procedure described above averaged the measured momentum for each event with the central momentum of the distribution. For events with large uncertainty in the measured

beam momentum, this procedure artificially reduced the width of the beam distribution. This then led to different cross sections for different beam settings. It can be shown that true beam distribution is restored by spreading out the contribution of each event with a Gaussian width equal to the fitted momentum uncertainty. This was done for both the τ 's and $\Lambda\pi^+\pi^-$ events, and resulted in changes in the cross section of as much as 10%. This procedure yielded good agreement between the cross sections calculated from different beam settings for each momentum interval.

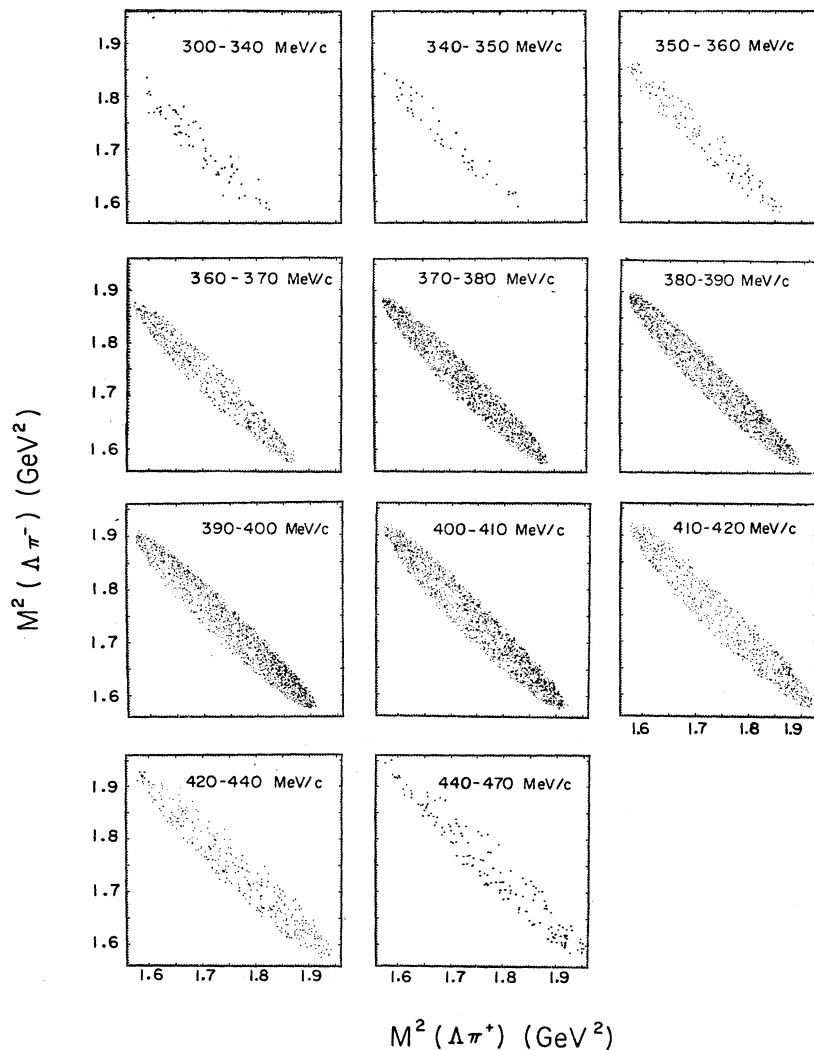


FIG. 5. Dalitz plots for $K^-p \rightarrow \Lambda\pi^+\pi^-$ at various incident K^- laboratory momenta. The abscissa (ordinate) corresponds to $\Lambda\pi^+$ ($\Lambda\pi^-$) invariant mass squared in GeV^2 .

III. SEMIQUANTITATIVE DESCRIPTION OF THE DATA

The momentum dependence of the partial cross section for $K^-p \rightarrow \Lambda \pi^+ \pi^-$ is shown in Fig. 4 and listed in Table I. The $\Lambda(1520)$ dominates the cross section in the region near 400 MeV/c, and a substantial background exists beyond this region. The two data points represented by circles are results from an experiment at higher energies.¹⁴ A quantitative separation of resonance and background contributions is given by the partial-wave analysis described in the following section.

Dalitz plots as a function of incident momentum are shown in Fig. 5. In the momentum interval from 360 to 420 MeV/c, bands of increased density at high $\Lambda\pi$ -invariant mass corresponding to $\Sigma(1385)$ production can be discerned. The center of the $\Sigma(1385)$ band occurs at an invariant mass squared of 1.92 (GeV)², which is outside the kinematically allowed region for all but the highest

momenta. The $\Sigma(1385)$ bands are accompanied by an enhancement in the low- $\pi\pi$ -mass region. This enhancement is generated by the constructive interference of the $\Sigma(1385)^+$ and $\Sigma(1385)^-$. The presence of the $\Sigma(1385)$ bands and the enhancement of low $\pi\pi$ masses can also be seen in the Dalitz-plot projections (Figs. 6, 7, and 8).

The constructive interference between $\Sigma(1385)^+$ and $\Sigma(1385)^-$ indicates the dominance of symmetric ($I=0$) production. Additional evidence for the dominance of the $I=0$ amplitude comes from some preliminary results on the reaction $K^-p \rightarrow \Lambda \pi^0 \pi^0$. An analysis is in progress of the zero-prong plus Λ topology from the same exposure. In order to separate the contributions from $\Lambda \pi^0$, $\Sigma \pi^0$, and $\Lambda \pi^0 \pi^0$ final states, a fit has been made to the angular distribution and polarization of the Λ as a function of the mass of the missing neutrals. Preliminary results indicate a cross section for $K^-p \rightarrow \Lambda \pi^0 \pi^0$ which is about half the $\Lambda \pi^+ \pi^-$ cross section at all incident momenta. This ratio is expected

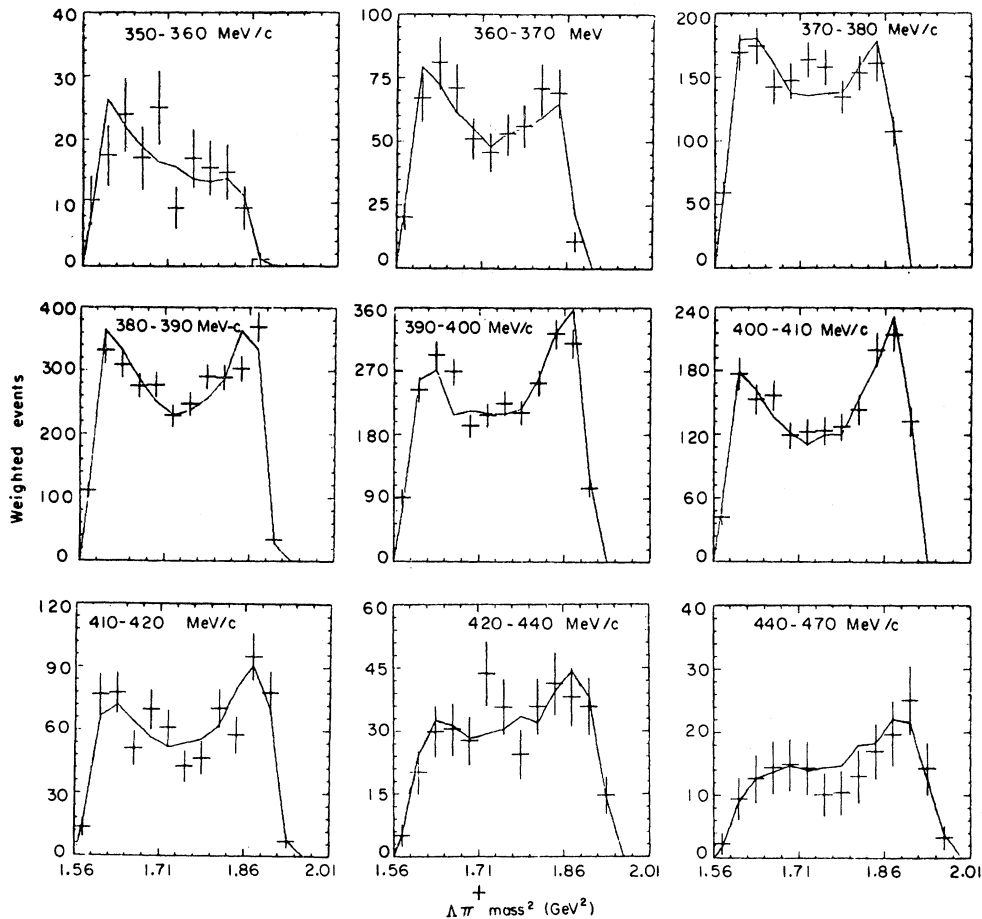


FIG. 6. $\Lambda\pi^+$ invariant-mass-squared distribution for various incident K^- momenta. The solid lines connect the results of a Monte Carlo prediction from the isobar model described in the text.

from pure $I=0$ production, so the $I=1$ contribution to the $\Lambda\pi^+\pi^-$ cross section must be small.

A more sensitive measure of the amount of $I=1$ production is given by the charge asymmetry of the Dalitz plot, shown as a function of incident momentum in Fig. 9. The asymmetry is defined as

$$\alpha = \frac{N^- - N^+}{N^- + N^+}, \quad (1)$$

where N^- is the number of events with a $\Lambda\pi^-$ -invariant mass larger than a $\Lambda\pi^+$ -invariant mass. This asymmetry can be generated by two effects. A mass difference between $\Sigma(1385)^-$ and $\Sigma(1385)^+$ introduces an asymmetry even when the amplitudes for their production are equal. In addition, the asymmetry can arise from the interference between $I=0$ and $I=1$ production. In the case of $\Sigma(1385)$ production, this corresponds to unequal production of $\Sigma(1385)^-$ and $\Sigma(1385)^+$. If the mass-

es of the $\Sigma(1385)^-$ and $\Sigma(1385)^+$ were equal, the asymmetry would be related to the isospin production amplitudes as follows:

$$\alpha = \frac{\sqrt{6} \operatorname{Re} \int M_0^* M_1 d\rho}{\int |M_0 + (\frac{3}{2})^{1/2} M_1|^2 d\rho}, \quad (2)$$

where the integral is over three-body phase space. An $I=1$ amplitude (M_1) about 10% as large as the $I=0$ amplitude (M_0) is sufficient to explain the observed structure. Thus the $I=1$ contribution to the partial cross section is of the order of a few percent.

The production angular distribution of the Λ with respect to the incident beam is shown as a function of incident momentum in Fig. 10. The distribution changes dramatically with momentum. It is forward peaked at 360 MeV/c, approaches a $(1 + 3 \cos^2\theta)$ distribution near 395 MeV/c, and becomes backward peaked at 430 MeV/c. A $(1 + 3 \cos^2\theta)$ distribution is expected from a pure

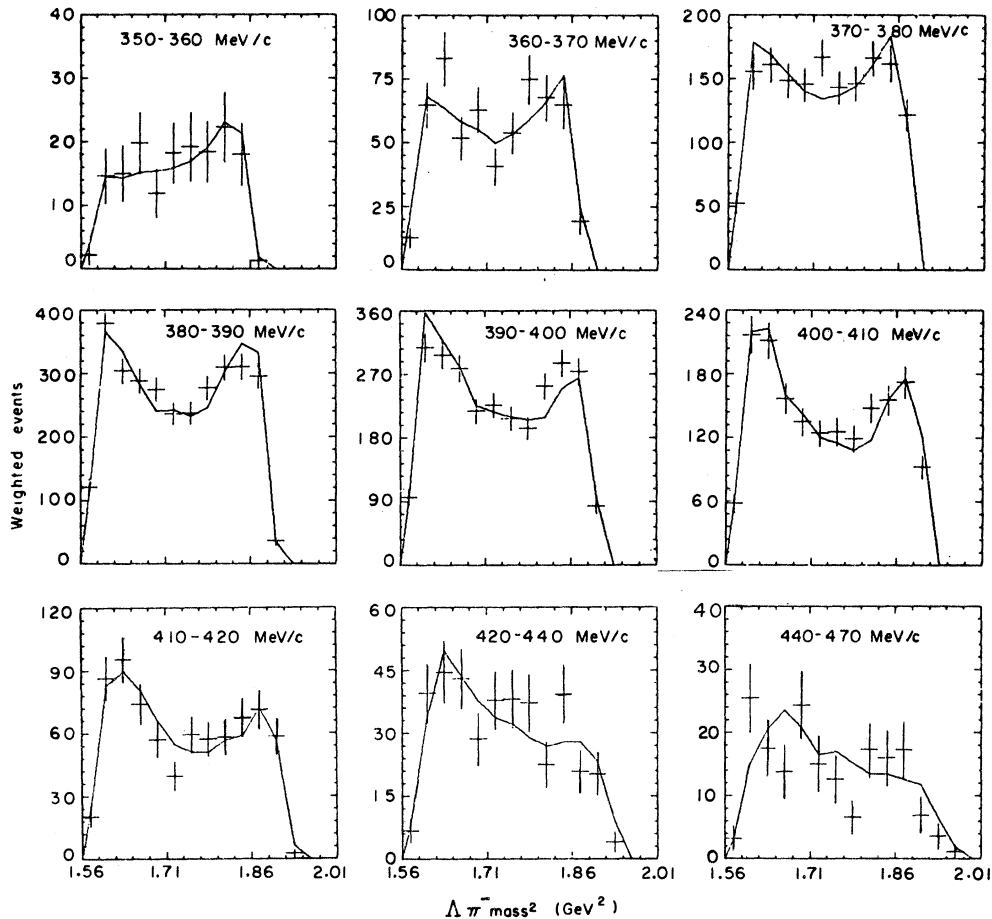


FIG. 7. $\Lambda\pi^-$ invariant-mass-squared distribution for various incident K^- momenta. The solid lines connect the results of a Monte Carlo prediction from the isobar model described in the text.

$J^P = \frac{3}{2}^+$ state decaying into $\frac{3}{2}^+$ and 0^- states. These angular distributions and the polarization of the Λ have been fitted to a Legendre polynomial expansion using a maximum-likelihood technique. The probability for each event is proportional to

$$1 + \sum_{i=1}^4 \frac{A_i}{A_0} P_i(\cos\theta) + \alpha_\Lambda \cos\beta \sum_{i=1}^4 \frac{B_i}{A_0} P_i'(\cos\theta). \quad (3)$$

Here

$$\cos\theta = \hat{K} \cdot \hat{\Lambda} \quad \text{and} \quad \cos\beta = \frac{\hat{K} \times \hat{\Lambda}}{|\hat{K} \times \hat{\Lambda}|} \cdot \hat{p},$$

where \hat{K} , $\hat{\Lambda}$, and \hat{p} are unit vectors in the direction of the K^- , Λ , and decay-proton momenta. The K^- and Λ momenta are defined in the over-all c.m. frame, and the decay proton is defined in the Λ rest frame. The weak-decay asymmetry α_Λ was set equal to 0.645. The A_i/A_0 and B_i/B_0 co-

efficients resulting from the fit are plotted as a function of incident momentum in Fig. 11. The polynomial fits are shown as curves over the data in Fig. 10. The dramatic changes in the angular distributions are reflected in the structure in A_1/A_0 and A_2/A_0 . If the entire cross section arose from $\Lambda(1520) \rightarrow \Sigma(1385)\pi$, then one would expect $A_2/A_0 = 1$. In fact this is nearly so in the vicinity of 390 MeV/c where $\Lambda(1520)$ is expected to dominate. However, the large structure in A_1/A_0 and the appreciable B_1/A_0 polarization coefficient show that even parity states are also present in significant amounts. A quantitative and simultaneous description of these angular distributions and the mass distributions is given by the isobar-model partial-wave analysis.

IV. PARTIAL-WAVE ANALYSIS

In order to separate the background from the $\Lambda(1520)$ production and to determine the modes of

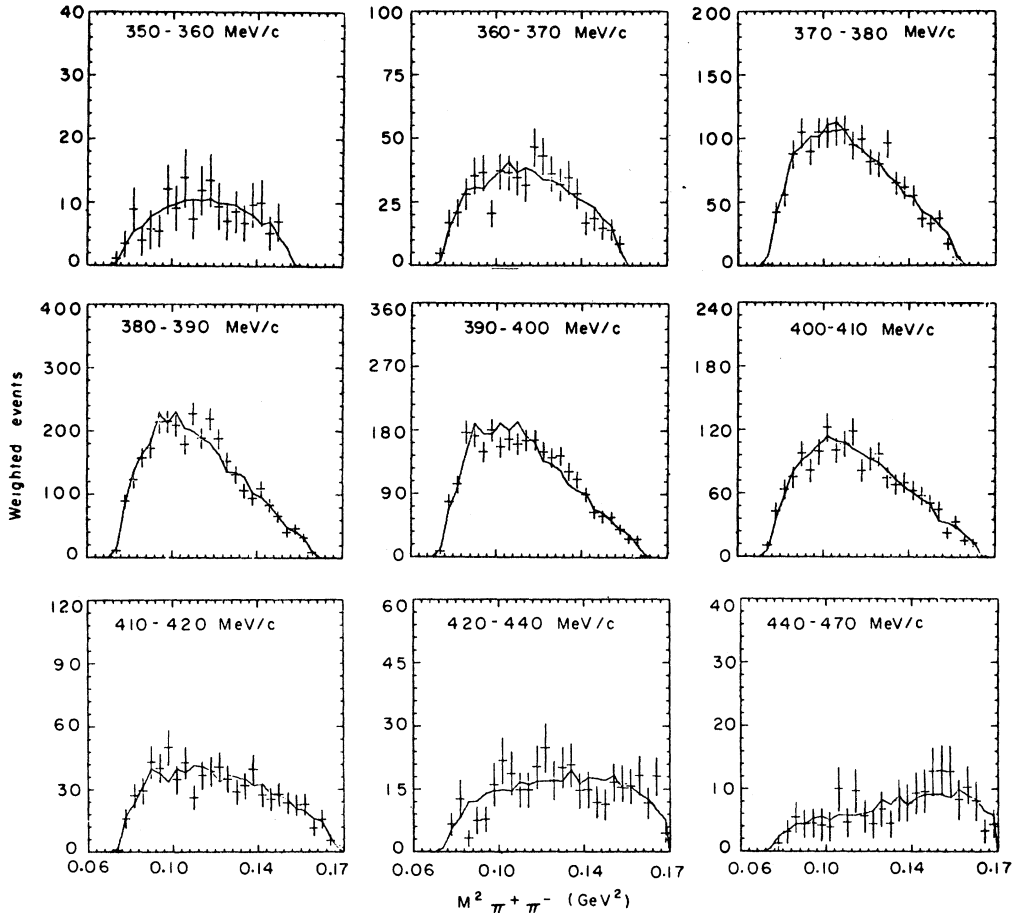


FIG. 8. $\pi^+ \pi^-$ invariant-mass-squared distribution for various incident K^- momenta. The solid lines connect the results of a Monte Carlo prediction from the isobar model described in the text.

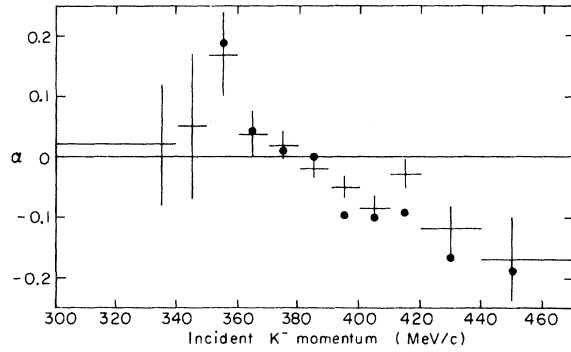


FIG. 9. The Dalitz-plot asymmetry as a function of incident K^- momentum. The asymmetry is $\alpha = (N^- - N^+) / (N^- + N^+)$, where N^- is the number of events with $\Lambda\pi^-$ -invariant mass larger than $\Lambda\pi^+$ -invariant mass. The dots are the predictions of the isobar-model fit described in the text.

the $\Lambda(1520)$ decay, we have fitted the data to an isobar model. The model treats the three-particle final state as the production of a particle and an isobar followed by the decay of the isobar, shown schematically in Fig. 12. The notation is defined in Table II. Four types of "isobars" have been chosen for this analysis:

- (1) a Λ and π resonating as $\Sigma(1385)$, denoted by " Y^* ,"
- (2) a Λ and π in a relative S wave, denoted by " $\Lambda\pi$,"
- (3) the two pions in a relative S wave, denoted by " σ ,"
- (4) the two pions in a relative P wave, denoted by " ρ ."

The incident and isobar-production waves chosen for this analysis are shown in Table III. Since the energy available in the final state is so low, only

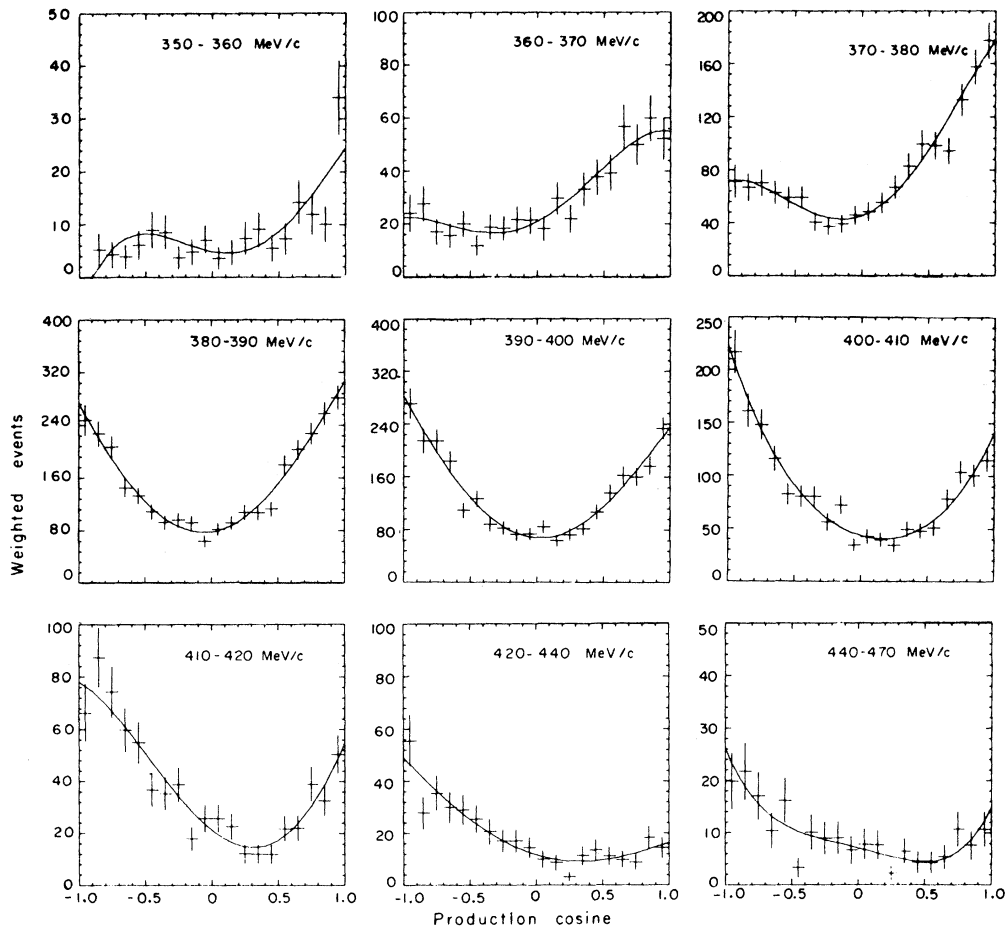


FIG. 10. The center-of-mass production cosine distribution of the Λ . The curves are the results of a Legendre-polynomial expansion fit to the production angular distribution and polarization at each incident momentum.

S and P waves have been used.

There are many formulations of the isobar model; Morgan gives a nice summary of the assumptions involved and a full list of references.¹⁵ For the most part we have followed the practical formulation of Deler and Valladas.¹⁶ The amplitude for the process indicated in Fig. 12, where particles 2 (π^+) and 3 (Λ) form the isobar, is written as a product of an energy-dependent factor and a factor describing the spin and angular-momentum decomposition:

$$A_{23}^{K\mu_f\mu_i} = T_{23}^K(E, m_{23}) f_{23}^{K\mu_f\mu_i}(\Omega_1, \Omega_f, \omega_{23}), \quad (4)$$

where K represents the quantum numbers J, L, L', j , and l , and assumes the values corresponding to the waves of Table III. The indices μ_f and μ_i refer to the incident proton and final Λ spin projections onto the axis of quantization. E is the center-of-mass energy, and m_{23} is the invariant mass of particles 2 and 3.

The energy-dependent factor accounts for angular-momentum barriers and final-state interactions of particles 2 and 3. The precise form that this factor should take is not well understood, and we have primarily followed the prescriptions used by Morgan in an analysis of $N\pi\pi$.¹⁵ The detailed energy dependence used for each of the four types of waves is described in the Appendix.

For the second factor, describing the spin and

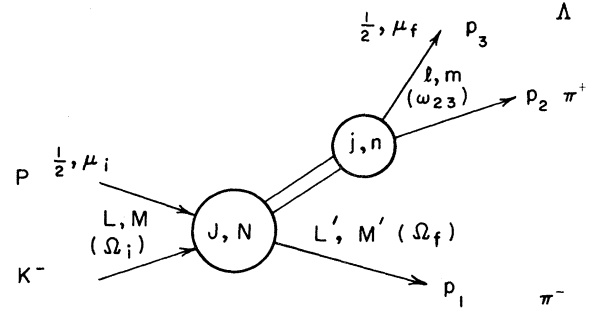


FIG. 12. Schematic diagram of the isobar-model description of the reaction $K^-p \rightarrow \Lambda \pi^+ \pi^-$. Particle 1, 2, and 3 refer to π^- , π^+ , and Λ . The notation is defined in Table II.

angular decomposition, we have followed the formulation of Deler and Valladas; the explicit formulas are described in the Appendix.

The amplitudes for the Y^* and $\Lambda\pi$ waves have been combined to form isospin-0 and isospin-1 amplitudes:

$$\begin{aligned} A_0^{K\mu_f\mu_i} &= \frac{1}{\sqrt{3}} (A_{23}^{K\mu_f\mu_i} + A_{13}^{K\mu_f\mu_i}), \\ A_1^{K\mu_f\mu_i} &= \frac{1}{\sqrt{2}} (A_{23}^{K\mu_f\mu_i} - A_{13}^{K\mu_f\mu_i}). \end{aligned} \quad (5)$$

Similar isospin combinations were made for the

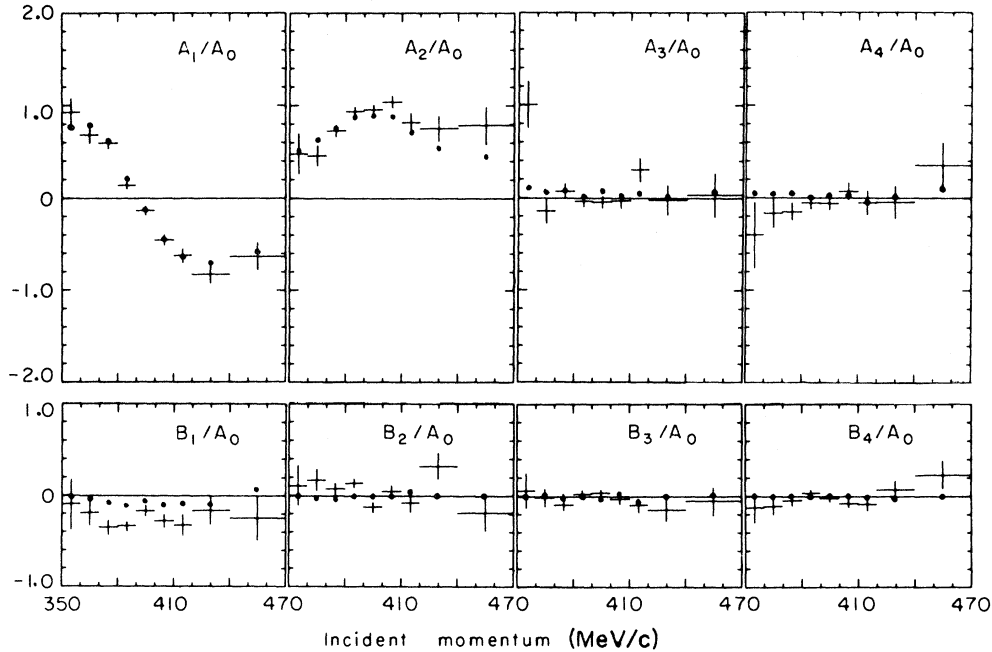


FIG. 11. The Legendre-polynomial coefficients from the fit to the Λ -production angular distribution and polarization. The dots correspond to the predictions of the isobar-model fit.

TABLE II. Variables used in isobar-model partial-wave analysis.^a

μ_i, μ_f = Initial proton and final Λ spin projections
L, M = Initial K^-p angular momentum and projection
J, N = Initial K^-p total spin and projection
L', M' = Angular momentum and projection between isobar and third particle
j, n = Spin and projection of the isobar
l, m = Angular momentum and projection between isobar decay particles
p_1, p_2, p_3 = Momentum of particles 1, 2, 3 in the over-all c.m. system
p'_i = Momentum of particle 2 or 3 in the rest frame of particles 2 and 3
E = Total energy in the three-particle rest frame
m_{ij} = Invariant mass of particles i and j
$\Omega_i = \Theta, \Phi$ = Polar and azimuthal angles of the incident beam with respect to the normal to the three-particle plane. The azimuth is defined from the Λ direction.
$\Omega_f = \frac{1}{2}\pi, \psi_Y$ = Polar and azimuthal angles of the isobar with respect to the normal to the three-particle plane
$\omega_{23} = \frac{1}{2}\pi, \psi_\Lambda$ = Polar and azimuthal angles of the Λ with respect to the normal to the three-particle plane
θ_1, θ_2 = Angle between pion 1, 2 and the Λ
θ_1^*, θ_2^* = Angle between the Λ and isobar in the isobar rest frame
μ_p = Spin projection of the Λ -decay proton
θ, ψ = Polar and azimuthal angles of the Λ -decay proton in the Λ rest frame

^a All angles are defined in the three-particle rest frame except those that are starred, which are defined in the appropriate diparticle rest frame.

$\pi\pi$ waves. The isospin amplitudes were normalized such that

$$\sum_{\mu_f \mu_i} \int |A_I^{K \mu_f \mu_i}|^2 d\rho = 4\pi \chi^2 (J + \frac{1}{2}), \quad (6)$$

where the integral is over the three-body phase space.

The decay of the Λ contains polarization information; this has been incorporated by constructing new amplitudes, $M_I^{K \mu_p \mu_i}$, which are linear combinations of the above A 's. μ_p is the spin projection of the Λ -decay proton, and θ and Ψ describe the orientation of the decay proton:

$$\begin{aligned} M_I^{K \frac{1}{2} \mu_i} &= A_I^{K(-\frac{1}{2}) \mu_i} (-P \sin \theta e^{-i\Psi}) \\ &\quad + A_I^{K \frac{1}{2} \mu_i} (S - P \cos \theta), \\ M_I^{K(-\frac{1}{2}) \mu_i} &= A_I^{K(-\frac{1}{2}) \mu_i} (S + P \cos \theta) \\ &\quad + A_I^{K \frac{1}{2} \mu_i} (-P \sin \theta e^{i\Psi}). \end{aligned} \quad (7)$$

S and P are the amplitudes describing the weak decay of the Λ ; they have been set real with a ratio $S/P = 2.735$ corresponding to an asymmetry of 0.645.¹⁷

In terms of these amplitudes the probability for each event is given by

$$\mathcal{P}(\Omega_i, \Omega_f, \omega_{23}, \omega_\Lambda, E, m_{23}) = \frac{|\sum_K a_K M_I^{K \mu_p \mu_i}|^2}{\int |\sum_K a_K M_I^{K \mu_p \mu_i}|^2 d\rho}, \quad (8)$$

where a_K are complex parameters. This probability has been used in an event-by-event likelihood

fit to the data.

The data were divided into nine bins of incident momentum (Table IV) and energy-independent fits were made to the data in each bin. The fitting was done with a CDC-6600 using the program OPTIME¹⁸ which varied the real and imaginary parts of a_K . The set of waves used at all momenta was chosen by preliminary fittings in the region of high statistics, 370 to 400 MeV/c. For these three bins the likelihoods for about 11 000 randomly generated

TABLE III. Waves used in partial-wave analysis.

K	Type	LL'12J
1	Y^*	DS03
2		DS13
3		PP01
4		PP11
5		PP03
6		PP13
7	$\Lambda\pi$	PS01
8		PS11
9		SP01
10		SP11
11		DP03
12		DP13
13	σ	PS01
14		SP01
15		DP03
16	ρ	SS11
17		DS13

TABLE IV. Events used in partial-wave analysis.

Bins	Momentum (MeV/c)	Number of events	Weighted number of events
1	350-360	129	161.5
2	360-370	484	597.0
3	370-380	1312	1570.5
4	380-390	2494	3073.2
5	390-400	2197	2718.8
6	400-410	1384	1717.7
7	410-420	615	750.0
8	420-440	314	383.8
9	440-470	163	191.6

“starting solutions” with all 17 waves of Table III were calculated. The four “starting solutions” with the highest likelihoods at each momentum were then optimized. Those waves with an amplitude less than 1 standard deviation from zero were rejected and the solution remaximized. Only those solutions where Y^*DS03 dominated gave high likelihoods with a small number of waves and reasonable continuity in momentum. The set of these solutions with the highest likelihoods included six waves and these were then used as starting solutions for the next lowest and highest momentum bins. In this way the solution was

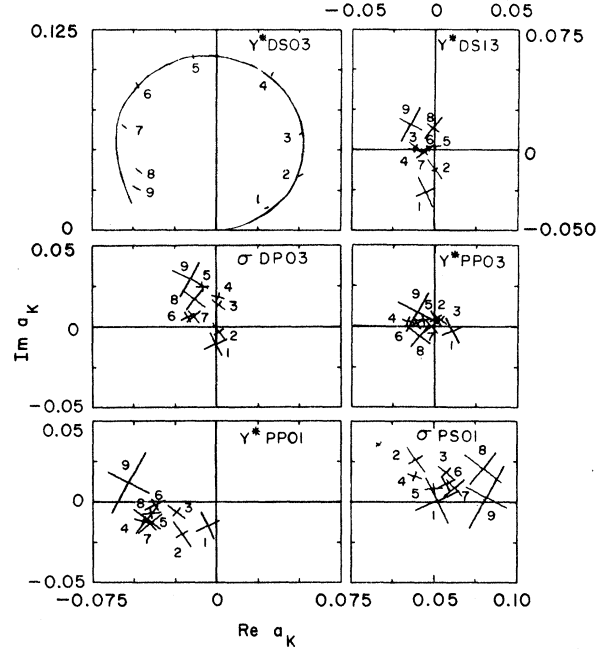


FIG. 13. Argand plots of the amplitudes from the isobar-model fit. The number refers to the incident momentum intervals defined in Table IV. The curve on the plot of Y^*DS03 is the prediction of a Breit-Wigner amplitude for the $\Lambda(1520)$.

TABLE V. Amplitudes from the isobar-model fit at each momentum. In the fitting the Y^*DS03 amplitude was fixed real. For the Argand plots of Fig. 13 the amplitudes have been rotated by δ , the phase of the Breit-Wigner distribution discussed in the text.

Momentum interval (MeV/c)	Y^*DS03		Y^*DS13		Y^*PP01		Y^*PP03		$\sigma PS01$		$\sigma DP03$		δ (radians)
	Re	Im	Re	Im	Re	Im	Re	Im	Re	Im	Re	Im	
350-360	0.034	0.000	-0.016	-0.021	-0.011	-0.011	0.009	-0.007	0.048	-0.021	-0.005	-0.010	0.437
	0.002	0.000	0.006	0.010	0.008	0.009	0.007	0.009	0.015	0.016	0.008	0.008	
360-370	0.062	0.000	-0.007	-0.010	-0.029	-0.005	0.003	0.004	0.047	0.000	-0.000	-0.004	0.593
	0.002	0.000	0.002	0.007	0.004	0.009	0.004	0.006	0.005	0.010	0.003	0.007	
370-380	0.079	0.000	-0.006	0.010	-0.020	0.014	0.006	-0.000	0.051	-0.032	0.011	0.008	0.869
	0.001	0.000	0.002	0.005	0.003	0.007	0.003	0.004	0.004	0.006	0.003	0.005	
380-390	0.103	0.000	-0.004	0.011	-0.026	0.038	-0.002	0.016	0.028	-0.031	0.018	0.005	1.239
	0.002	0.000	0.002	0.004	0.003	0.006	0.003	0.004	0.003	0.005	0.003	0.004	
390-400	0.109	0.000	0.002	-0.000	-0.002	0.040	0.005	0.006	0.002	-0.051	0.026	0.005	1.703
	0.002	0.000	0.002	0.004	0.003	0.006	0.003	0.004	0.004	0.005	0.003	0.004	
400-410	0.102	0.000	0.003	0.003	0.016	0.034	0.007	0.009	-0.017	-0.056	0.013	0.012	2.055
	0.002	0.000	0.002	0.005	0.004	0.007	0.004	0.005	0.005	0.006	0.004	0.005	
410-420	0.085	0.000	0.003	0.006	0.016	0.039	0.001	0.001	-0.034	-0.053	0.014	0.006	2.281
	0.002	0.000	0.003	0.006	0.006	0.009	0.006	0.006	0.007	0.008	0.005	0.005	
420-440	0.060	0.000	0.009	-0.010	0.026	0.035	0.003	0.010	-0.050	-0.066	0.021	-0.005	2.472
	0.002	0.000	0.005	0.009	0.010	0.011	0.008	0.009	0.014	0.013	0.008	0.008	
440-470	0.055	0.000	0.020	-0.007	0.052	0.015	0.013	-0.003	-0.070	-0.042	0.028	-0.018	2.641
	0.003	0.000	0.008	0.012	0.014	0.021	0.013	0.014	0.014	0.022	0.012	0.012	

propagated from momentum to momentum. The amplitudes thus achieved are plotted in the Argand diagrams of Fig. 13 and listed in Table V. The continuity achieved by the propagation of solutions is reasonable.

Since there is an over-all free phase at each momentum, the amplitude for $Y^*D S03$ was chosen to correspond to the phase of a $\Lambda(1520)$ Breit-Wigner discussed below. The over-all scale of the amplitudes is determined from the measured cross sections of Table I. We emphasize, however, that the relative amount of each wave at each momentum is freely determined by the fit. Thus, in addition to the reasonable continuity of the smaller waves, there is very good agreement of the $Y^*D S03$ amplitude with the $\Lambda(1520)$ Breit-Wigner, shown as a curve in Fig. 13(a).

The total width for the Breit-Wigner form used includes D -wave barriers (with a radius of interaction of 1 fm) for the $\bar{K}N$ and $\Sigma\pi$ partial widths. The partial width for $\Lambda(1520) \rightarrow \Sigma(1385)\pi$ contains only an effective phase-space factor since the reaction proceeds through a final S wave. The effective phase space was taken to be the integral of the isobar-model amplitude $Y^*D S03$. This is essentially equivalent to averaging the relative momentum of the $\Sigma(1385)\pi$ system over the P -wave Breit-Wigner shape of the $\Sigma(1385)$. The good agreement with the energy-independent points in Fig. 13(a) confirms the momentum dependence of the $\Lambda(1520)$ Breit-Wigner form.

The $Y^*D S13$ wave is the only wave with isospin = 1. This wave is very small and shows no obvious continuous pattern from momentum to momentum. The $Y^*P P01$ amplitude contributes significantly and tends to grow with momentum. The $Y^*P P03$ is small and shows no continuous behavior. The $\sigma P S01$ is the major background wave and remains approximately fixed. This wave, with all particles in a relative S wave, represents the usual "phase-space" background contribution. Finally the $\sigma D P03$ amplitude is small. It represents the non- $\Sigma(1385)$ component of the $D03$, $\Lambda(1520)$. Within the errors and uncertainty in the model, this $\sigma D P03$ amplitude varies roughly as a Breit-Wigner. The final fit involves no waves of the " $\Lambda\pi$ " or " ρ " types. However, substituting the $\Lambda\pi P S01$ and $\Lambda\pi D P03$ for the $\sigma P S01$ and the $\sigma D P03$ made essentially no change in the amplitudes and only slightly lowered the likelihood. Thus the data cannot distinguish between the slightly different mass distributions predicted by the two types of waves.

Considering the many assumptions involved in the isobar model, the small waves here probably have little physical significance; more than likely they represent the mismatch between the data and the model. The large waves hopefully are repre-

TABLE VI. χ^2 values from the $\Lambda\pi^+$, $\Lambda\pi^-$, and $\pi^+\pi^-$ mass projections.

Momentum interval (MeV/c)	$\Lambda\pi^+$	$\Lambda\pi^-$	$\pi^+\pi^-$
350-360	11.0	3.7	10.4
360-370	14.8	17.5	21.1
370-380	11.4	11.0	40.1
380-390	22.6	16.9	28.1
390-400	25.1	19.8	33.7
400-410	9.2	13.7	20.5
410-420	19.0	12.8	21.1
420-440	8.7	15.7	44.5
440-470	5.7	28.3	14.2
Total	128	139	234
Total data points	113	113	207

sending the physical behavior of the reaction.

In order to illustrate the agreement between the fit and the data, a set of Monte Carlo events were generated isotropically in phase space and then weighted with the probability of Eq. (8), using the final parameters from the fit. The $\Lambda\pi$ and $\pi\pi$ mass distributions thus predicted are shown as curves over the data in Figs. 6, 7, and 8. The fit accurately reproduces the mass distributions at each momentum. The χ^2 for each plot is shown in Table VI.

The Dalitz-plot asymmetry from the fit is in good agreement with the data, as shown in Fig. 9. The amount of this asymmetry that comes from the $\Sigma(1385)^-\Sigma(1385)^+$ mass difference was investigated by generating a set of Monte Carlo events without the $I=1$ amplitude $Y^*D S13$. The resulting asymmetry was equal to -0.06 and essentially independent of incident momentum in the region of interest.

Finally, the Monte Carlo events were fitted with the probability of Eq. (3) in order to find A_i and B_i and compare them with those from the data. The Monte Carlo results are shown as dots in Fig. 11. The agreement with the major structure in A_1/A_0 and A_2/A_0 is very good. However, there is disagreement with the polarization. Although the fit yielded some B_1/A_0 with the correct sign, it systematically failed to provide enough. In addition, we should emphasize that the B coefficients used for the comparison only describe one component of the Λ polarization. The isobar model describes the whole polarization vector, and the fit uses all the polarization information from the data. However, because of the particular waves involved, the component described by the B 's is expected to be the most important.

V. CONCLUSIONS

Our conclusion from the fitting is that the $\Lambda \pi^+ \pi^-$ final state of the $\Lambda(1520)$ is dominated by $\Sigma(1385)\pi$. This is made more quantitative by considering the cross sections from the two D waves coming from the $\Lambda(1520)$, the Y^*DS03 , and the $\sigma DP03$. The contributions to the cross section of each of these waves and their interference are plotted in Fig. 14. All three contributions are seen to peak at 395 MeV/c. The ratio of the Y^*DS03 cross section to the total cross section coming from the $\Lambda(1520)$

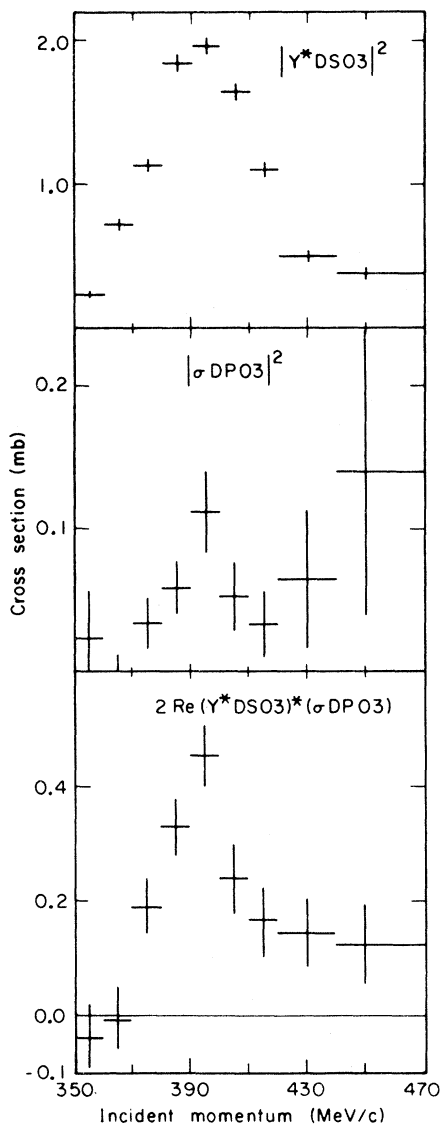


FIG. 14. Partial cross sections (millibarns) for the only two waves with an incident D wave. Both waves (Y^*DS03 and $\sigma DP03$) peak near 395 MeV/c, the momentum required to form the $\Lambda(1520)$. Note the difference in scales.

is given in Fig. 15. The fraction due to Y^*DS03 remains constant throughout the $\Lambda(1520)$ region at a value of about 0.82. Averaging over the five momentum intervals centered on the $\Lambda(1520)$ (intervals 3–7), the final value for the branching fraction

$$[\Lambda(1520) \rightarrow \Sigma(1385)\pi \rightarrow \Lambda \pi \pi] / [\Lambda(1520) \rightarrow \text{all } \Lambda \pi \pi]$$

is 0.82 ± 0.10 . The error has been estimated by varying some of the input parameters to the model and by studying the sensitivity of the branching fraction to the inclusion of different sets of amplitudes consistent with a reasonable energy continuity. Reasonable variations of the masses and widths of the $\Sigma(1385)$ did not significantly affect the results. For example, increasing the width of the $\Sigma(1385)$ from 40 to 45 MeV increased the branching fraction by 0.03. Inclusion of different amplitudes for the smaller background waves changed the branching fraction by ± 0.03 .

This branching fraction is in agreement with the result from the formation experiment of Ref. 3. The latter experiment was able to fit the $M^2 \Lambda \pi$ mass distributions and some angular distributions with a set of isobar waves which included only one wave corresponding to $\Lambda(1520)$ production, the Y^*DS03 .

Our result for the branching fraction disagrees strongly with the result 0.39 ± 0.10 quoted from the production experiment of Burkhardt *et al.*⁵ The production experiment has many fewer events (206 events) than the present experiment and has the additional problem of extracting the $\Lambda(1520)$ signal from the $\Lambda \pi^+ \pi^- \pi^0$ final states. They divide the data into three mass intervals centered on the $\Lambda(1520)$. The data in the central interval (with about 15% background) agree with ours and yield

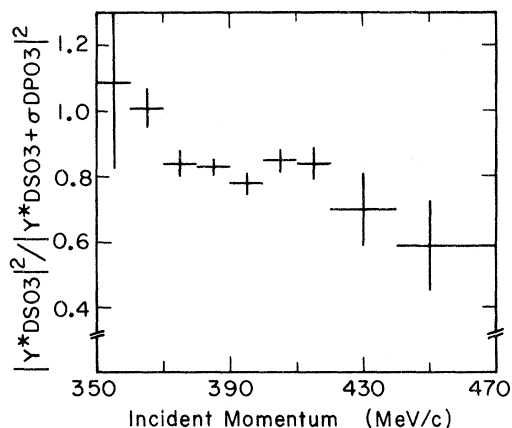


FIG. 15. The ratio of the cross section for Y^*DS03 to the sum of the cross sections for Y^*DS03 and $\sigma DP03$ as a function of incident momentum.

a branching fraction consistent with ours. The data in the side intervals (with about 30% background) yield lower branching fractions and contribute to their low over-all value, thus perhaps explaining the discrepancy.

At the resonance energy the contribution to the $\Lambda\pi^+\pi^-$ cross section from $\Lambda(1520)$ production is 2.53 mb (Fig. 14). Using this cross section and an elasticity for the $\Lambda(1520)$ of 0.46 ± 0.02 we calculate a branching fraction for the $\Lambda(1520)$ into $\Lambda\pi\pi$ (all charge states) of $(11 \pm 1)\%$. This value agrees with the world average $(9.6 \pm 0.7)\%$ and disagrees with the result from the analysis of Ref. 3 which found only 1.25 mb coming from the $\Lambda(1520)$ and a branching fraction of $4.1 \pm 0.5\%$.

Finally, taking the world average value of 16 ± 2 MeV for the $\Lambda(1520)$ total width,¹⁹ we calculate a width for $\Lambda(1520) \rightarrow \Sigma(1385)\pi$ of 1.40 ± 0.26 MeV.

VI. SU(3) IMPLICATIONS

The information presently known about the $J^P = \frac{3}{2}^-$ baryons is listed in Table VII. Previous

analyses of these baryons have ordered the first five states into a singlet and an octet.^{1,2} With the data known at the time, this treatment was successful. By invoking configuration mixing between the $\Lambda(1520)$ and $\Lambda(1690)$, these analyses were able to derive mixing angles from (a) the Gell-Mann-Okubo mass relation, (b) the D -wave decays into baryon octet and meson octet, and (c) the S -wave decays into baryon decuplet and meson octet. The mixing angles derived from these three independent methods were in agreement.

We now reexamine this situation in the light of present experimental knowledge of these baryons and the results of this experiment. The physical $\Lambda(1520)$ and $\Lambda(1690)$ states are related to the pure singlet and octet states as follows:

$$\begin{aligned} |(1520)\rangle &= \cos\theta |1\rangle - \sin\theta |8\rangle, \\ |(1690)\rangle &= +\sin\theta |1\rangle + \cos\theta |8\rangle. \end{aligned} \quad (9)$$

The Gell-Mann-Okubo mass relation gives the

TABLE VII. Properties of $J^P = \frac{3}{2}^-$ baryons.^a

Resonance	Mass (MeV)	Total width (MeV)	Decay modes	Branching fraction X	Remarks
$\Lambda(1520)$	1518 ± 2	16 ± 2	$N\bar{K}$ $\Sigma\pi$ $\Sigma(1385)\pi$	0.46 ± 0.01 0.41 ± 0.01 0.093 ± 0.006	
$\Lambda(1690)$	1690 ± 10	27 to 85	$N\bar{K}$ $\Sigma\pi$ $\Sigma(1385)\pi$	~ 30 ~ 40 0.005 to 0.04	
$N(1520)$	1510 to 1540	105 to 150	$N\pi$ $N\pi\pi$ $N\eta$	~ 50 ~ 50 ~ 0.6	Dominated by $\Delta(1236)\pi$
$\Sigma(1670)$	1660 to 1680	50 ± 10	$N\bar{K}$ $\Sigma\pi$ $\Lambda\pi$ $\Sigma(1385)\pi$	~ 0.08	The experimental situation is confused. There is probably more than one $\frac{3}{2}^-$ state $X_{N\bar{K}} X_{\Sigma(1385)\pi} = 0.031 \pm 0.006$
$\Xi(1820)$	1795 to 1870	50 to 100	$\Xi\pi$ $\Sigma\bar{K}$ $\Lambda\bar{K}$		
$\Delta(1670)$	1650 to 1720	175 to 300	$\Delta\pi$ $N\pi$	0.15 ± 0.03	
$N(1700)$	1600 to 1730				Only poor evidence from partial-wave analysis
$\Sigma(1940)$	1940 ± 22	235 ± 28	$N\bar{K}$ $\Lambda\pi$ $\Sigma\pi$	$(X_{N\bar{K}} X_{\Lambda\pi})^{1/2} = 0.13 \pm 0.03$ $(X_{N\bar{K}} X_{\Sigma\pi})^{1/2} = 0.12 \pm 0.03$	
$\Lambda(2010)$	1980 to 2040	80 to 180	$N\bar{K}$ $\Sigma\pi$		Seen in only one partial-wave analysis $(X_{N\bar{K}} X_{\Sigma\pi})^{1/2} = 0.20 \pm 0.04$
$N(2040)$	2040 ± 11	274 ± 24	$N\pi$	0.17 ± 0.06	

^a From Ref. 17.

mixing angle in terms of the masses:

$$\cos^2 \theta = \frac{m_\Xi - m_{1520}}{m_{1690} - m_{1520}}, \quad (10)$$

where $m_\Xi = \frac{1}{3}(2m_N - 2m_\Sigma - m_\Xi)$. In fact, this relation is not a very strong constraint on the mixing angle, largely due to the considerable uncertainty in the Ξ mass. Previous analyses optimistically chose the mass to be 1819 ± 6 MeV and found a mixing angle of $21^\circ \pm 4^\circ$.¹ However, a more conservative choice which reflects the confused experimental situation would be $m_\Xi = 1832 \pm 37$. The resulting mixing angle is $|\theta| = 13^\circ \pm 22^\circ$.²⁰

The D -wave decays of the singlet and octet have been recently summarized by Plane *et al.*² Using the decay rates into stable baryons and mesons, they perform a fit to derive the F and D coupling constants and the mixing angle. No information about the Ξ state was used in the fit. With 5 degrees of freedom they found $\chi^2 = 0.8$ and a mixing angle $\theta = -25^\circ \pm 6^\circ$.

Data on decays into decuplet plus pion via the S wave are slowly becoming available.³⁻⁶ Previous analyses were based on rough limits.^{1,5} The $SU(3)$ prediction relates the coupling constants and mixing angle, so some assumption must be made to relate the experimentally measured partial widths and the coupling constants. The usual prescription for decay into stable particles is the potential-theory relation, which for S -wave decay is

$$\Gamma = C^2 g^2 p \frac{M_N}{M_R}. \quad (11)$$

Here C is an $SU(3)$ Clebsch-Gordan coefficient, M_R and M_N are the resonance and nucleon masses, and p is the c.m. momentum of the decay products. The factor p/M_R represents the phase space available to the decay. For a decay into unstable particles this should be replaced by an integral over the phase space of the matrix element squared.

The following formula has been adopted:

$$\Gamma = C^2 g^2 I, \quad \text{where } I = \int |Y^*DS03|^2 d\rho. \quad (12)$$

The integral I as a function of incident momentum in the region of the $\Lambda(1520)$ and the $\Lambda(1690)$ is shown in Fig. 16. The increased fraction of $\Sigma(1385)$, which lies in the physical region as the energy increases, accounts for the rapid increase in I compared with three-body phase space, the curve labeled ρ in Fig. 16.

The partial widths for the S -wave decays of $\Lambda(1520)$ and $\Lambda(1690)$ can be used to determine the mixing angle. Using Eq. (9) and the fact that an $SU(3)$ singlet is forbidden to decay to $\Sigma(1385)\pi$, we derive

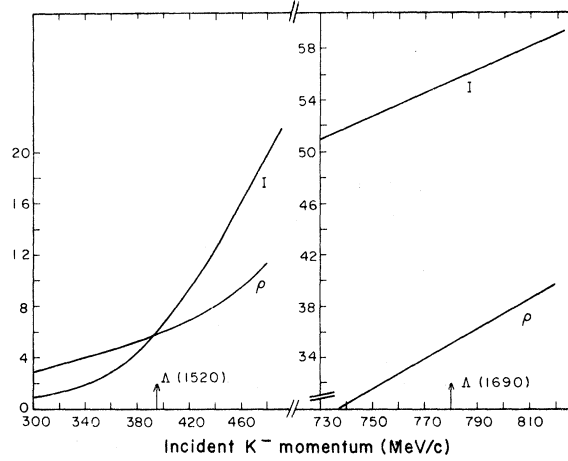


FIG. 16. The integral of the Y^*DS03 amplitude squared (I) and the integral of the $\Lambda\pi^+\pi^-$ phase space (ρ) as a function of incident K^- momentum in the region of the $\Lambda(1520)$ and in the region of the $\Lambda(1690)$. The same (arbitrary) scale is used in both regions.

$$\tan^2 \theta = \frac{\Gamma_{1520}}{\Gamma_{1690}} \frac{I_{1690}}{I_{1520}}. \quad (13)$$

Previous estimates for the partial width for $\Lambda(1690) \rightarrow \Sigma(1385)\pi$ were based on an upper limit of about 10 MeV.⁴ However, a recent analysis with increased statistics yields a very small amplitude for the decay, 0.06.⁸ Assuming an elasticity of 0.2 and a total width of 55 MeV,¹⁷ this amplitude implies a partial width into $\Sigma(1385)\pi$ of 1.0 MeV. However, there is an estimated uncertainty of 0.03 on the amplitude,²¹ and there is a large uncertainty in the total width of about 30 MeV. These large uncertainties allow values for the partial width from 0.1 to 3.44 MeV.

With I_{1690}/I_{1520} equal to 9.54 (Ref. 22) and Γ_{1520} equal to 1.40 MeV, we have used Eq. (13) to calculate $|\theta|$ for these limits on the Γ_{1690} partial width. With $\Gamma_{1690} = 0.1$ MeV, $|\theta|$ equals 84° ; and with $\Gamma_{1690} = 3.44$ MeV, $|\theta|$ equals 63° . In order to obtain agreement with the mixing angle from the D -wave decays ($\theta = -25^\circ$), the partial width for the $\Lambda(1690)$ would have to be 62 MeV. In the light of this large discrepancy, the simple singlet-octet description of these decays no longer appears to be valid.

A possible explanation of the discrepancy may be due to a misassignment of the currently observed states. More detailed data on all states in this energy region are required to test this hypothesis.

Alternatively, the discrepancy may come from a failure of the prescription used to account for mass differences. Using the available phase space to account for mass differences is the traditional prescription used in all previous comparisons with

SU(3). The success of this prescription has been truly remarkable. However, there is no fundamental reason to believe the phase space alone should account for the SU(3) breaking. Perhaps the prescription fails in the example considered here.

With the abandonment of the simple singlet-octet picture, the situation rapidly becomes complicated. Turning to the quark model,²³ which has had considerable success in accounting for the baryon states, we find predictions for two $J^P = \frac{3}{2}^-$ octets and one $\frac{3}{2}^-$ decuplet. However, experimental information on these states is very sketchy. As indicated in Table VII, possible members of the second octet and the decuplet have been seen. However, the last three states have masses too high to be plausibly associated with the missing octet and they are usually regarded to arise from radial excitations. In terms of the quark model there can be spin-orbit mixing of the two octets, and in addition there can be mixing of the decuplet with the two octets by SU(3)-breaking forces. On the basis of a specific model for quark interactions, Faiman has estimated the possible mixing between the octets and singlet.²⁴ Treating the baryon resonances as bound states of three paraquarks interacting via harmonic-oscillator forces, he derives two possible singlet-octet mixing angles for the $\Lambda(1520)$, $\theta = 63^\circ$ and $\theta = 75^\circ$. With new data becoming available on the decays of $\frac{3}{2}^-$ states into decuplets and pions, further constraints will be imposed on possible multiplet members and realistic tests of specific models may become available.

ACKNOWLEDGMENTS

We express our appreciation to Dr. Joseph Murray and Roger Gearhart for their valuable contributions to the initial phases of the experiment. We also wish to thank the 25-in. bubble-chamber crew and our scanning and measuring staff for their conscientious assistance. David Herndon, Larry Miller, and especially Werner Koellner provided valuable assistance with the computer programming of the isobar-model fits. We gratefully acknowledge helpful discussion with Dr. Gerard Smadja. It is a pleasure to acknowledge the support of Professor Luis W. Alvarez.

APPENDIX: ISOBAR-MODEL FORMULAS

In this appendix we define in detail the two factors in the isobar-model amplitudes used in Eq. (4) of the text.

The energy-dependent factor T_{23} describes the amplitude for an "isobar" formed with particles 2 and 3. In general, it contains an angular-momen-

tum barrier for the production of the isobar and a final-state factor describing the interactions of particles 2 and 3. The latter factor is either a Breit-Wigner form or a Watson final-state factor, depending on the type of wave involved. The following equations define T_{23} for each of the four types of waves used in the analysis. The variables are defined in Table II and Fig. 12:

For " Y^* ,"

$$T_{23} = \frac{1}{(p_1 p_1')^{1/2}} \frac{\sqrt{\Gamma}}{m_{23} - m_R + \frac{1}{2}i\Gamma} B(p_1, L'), \quad (14)$$

where

$$B(p_1, L') = \left(\frac{p_1^{2L'+1}}{(1 + p_1^2 R^2)^{L'}} \right)^{1/2}$$

and R , the radius of interaction, was chosen to be 1 F. The resonance parameters chosen for the $\Sigma(1385)$ were as follows:

$$\begin{aligned} m_R[\Sigma^+(1385)] &= 1.384 \text{ GeV}, \\ m_R[\Sigma^-(1385)] &= 1.388 \text{ GeV}, \end{aligned} \quad (15)$$

and $\Gamma = 9.3(p_1')^3/[1 + (Rp_1')^2]$, corresponding to a width of 0.040 GeV, at the resonant energy.

For " $\Lambda\pi$,"

$$T_{23} = \frac{1}{(p_1 p_1')^{1/2}} \frac{e^{i\delta} \sin\delta}{(p_1')^{L'+1/2}} B(p_1, L') \quad (16)$$

and $\delta = 2.88(m_{23} - 1.255)$. This parametrization of the $\Lambda\pi$ S-wave phase shift has been taken from the K -matrix analysis of low-energy $\bar{K}N$ scattering by Martin and Sakitt.²⁵

For " σ ,"

$$T_{12} = \frac{1}{(p_3 p_3')^{1/2}} \frac{e^{i\delta} \sin\delta}{(p_3')^{1/2}} B(p_3, L') \quad (17)$$

and

$$p_3' \cot\delta = m_{12} \left(\frac{1}{0.32} - 109.5(p_3')^2 + 1114(p_3')^4 \right).$$

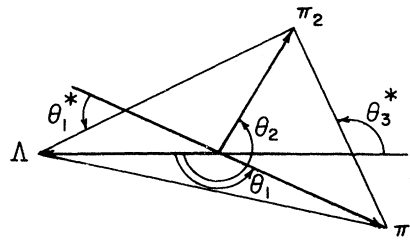


FIG. 17. Diagram defining the angles used in the isobar model. The notation is defined in Table II.

For “ ρ ,”

$$T_{12} = \frac{1}{(p_3 p_3')^{1/2}} \frac{e^{i\delta} \sin\delta}{(p_3')^{1/2}} B(p_3, L') \quad (18)$$

and

$$(p_3')^3 \cot\delta = \frac{m_{12}}{2} \left(\frac{1 - 0.1609(p_3'/m_\pi)^2}{1.375} \right).$$

The $I=0$ parametrization corresponds to a scatter-

ing length of $0.16 m_\pi^{-1}$.¹⁵ The $I=1$ phase shift corresponds to a resonance of mass equal to 0.750 GeV and width equal to 0.100 GeV.¹⁴

The formulas for the spin and angular-momentum dependence are the same as those derived by Deler and Valladas. We quote here an especially simple formulation. The angles and spin are defined in Table II and Figs. 12 and 17.

$$f^{K\mu_f\mu_i}(\Omega_i, \Omega_f, \omega_{23}) = \sum_{MM'Nnm} \langle LM\frac{1}{2}\mu_i | JN \rangle \langle JN | L'M'jn \rangle \langle jn | l m \frac{1}{2}\mu_f \rangle Y_L^{M*}(\theta, \Phi) Y_L^{M'}(\frac{1}{2}\pi, \Psi_Y) Y_1^m(\frac{1}{2}\pi, \Psi_\Lambda), \quad (19)$$

where $\Psi_Y = \pi + \theta_1$, $\Psi_\Lambda = \pi + \theta_1 + \theta_1^*$, and $K \sim JLL'jl$. For “ σ ”- and “ ρ ”- type waves, a slightly different form is required:

$$f^{K\mu_f\mu_i}(\Omega_i, \Omega_f, \omega_{12}) = \sum_{MM'\mathcal{J}\mathcal{M}m} \langle LM\frac{1}{2}\mu_i | JN \rangle \langle JN | \mathcal{J}\mathcal{M}lm \rangle \langle \mathcal{J}\mathcal{M} | L'M'\frac{1}{2}\mu_f \rangle Y_L^{M*}(\theta, \Phi) Y_L^{M'}(\frac{1}{2}\pi, \Psi_\sigma) Y_1^m(\frac{1}{2}\pi, \Psi_2), \quad (20)$$

where $\Psi_\sigma = \pi$ and $\Psi_2 = \pi + \theta_2^*$. \mathcal{J} and \mathcal{M} are the spin and projection resulting from coupling the spin of the Λ and the relative angular momentum between the Λ and $\pi\pi$ system.

The amplitudes formed from these factors T and f were normalized according to Eq. (6) of the text.

*Work done under the auspices of the U. S. Atomic Energy Commission.

¹R. Levi-Setti, in *Proceedings of the Fifth International Conference on Elementary Particles, Lund, 1969*, edited by G. von Dardel (Berlingska Boktryckeriet, Lund, Sweden, 1970), p. 339; E. Burkhardt, H. Filthuth, E. Kluge, H. Oberlack, R. R. Ross, B. Conforto, D. M. Harmsen, T. Lasinski, R. Levi-Setti, M. Raymond, R. Armenteros, M. Ferro-Luzzi, D. W. G. S. Leith, A. Minten, R. D. Tripp, R. Barloutaud, P. Granet, J. Meyer, and J. P. Porte, Nucl. Phys. **B14**, 106 (1969).

²D. E. Plane, P. Baillon, C. Bricman, M. Ferro-Luzzi, J. Meyer, E. Pagiola, N. Schmitz, E. Burkhardt, H. Filthuth, E. Kluge, H. Oberlack, R. Barloutaud, P. Granet, J. P. Porte, and J. Prevost, Nucl. Phys. **B22**, 93 (1970).

³Shu-bon Chan *et al.*, Phys. Rev. Letters **28**, 256 (1972).

⁴J. H. Bartley, R. Y. L. Chu, R. M. Dowd, A. F. Greene, J. Schneps, W. H. Sims, J. R. Albright, E. B. Brucker, J. Lannutti, B. G. Reynolds, M. Meer, J. E. Mueller, M. Schneeberger, and S. E. Wolf, Phys. Rev. Letters **21**, 1111 (1968).

⁵E. Burkhardt, H. Filthuth, E. Kluge, H. Oberlack, R. Armenteros, M. Ferro-Luzzi, D. W. G. S. Leith, R. Levi-Setti, J. Meyer, A. Minten, R. Barloutaud, P. Granet, and J. P. Porte, Nucl. Phys. **B27**, 64 (1971).

⁶J. Prevost *et al.*, reported by R. Barloutaud, in *Proceedings of the Amsterdam International Conference on Elementary Particles, 1971*, edited by A. G. Tenner and M. Veltman (North-Holland, Amsterdam, 1972).

⁷The results of this experiment have been briefly described in Phys. Rev. Letters **28**, 1220 (1972).

⁸M. B. Watson, M. Ferro-Luzzi, and R. D. Tripp, Phys. Rev. **131**, 2248 (1963).

⁹Roger O. Bangerter, Lawrence Radiation Laboratory, Alvarez Group Physics Note No. 574, 1965 (unpublished).

¹⁰T. S. Mast, M. Alston-Garnjost, R. O. Bangerter, A. Barbaro-Galtieri, F. T. Solmitz, and R. D. Tripp, Lawrence Berkeley Laboratory Report No. LBL 301, 1971 (unpublished).

¹¹T. S. Mast, L. K. Gershwin, M. Alston-Garnjost, R. O. Bangerter, A. Barbaro-Galtieri, J. J. Murray, F. T. Solmitz, and R. D. Tripp, Phys. Rev. **183**, 1200 (1969).

¹²Stephen E. Derenzo and Roger H. Hildebrand, Lawrence Radiation Laboratory Report No. UCRL-18638, 1968 (unpublished).

¹³Roger Bangerter and Terry Mast, Lawrence Berkeley Laboratory, Alvarez Group Physics Note No. 731, 1971 (unpublished).

¹⁴R. Armenteros, P. Baillon, C. Bricman, M. Ferro-Luzzi, E. Pagiola, J. O. Petersen, D. E. Plane, N. Schmitz, E. Burkhardt, H. Filthuth, E. Kluge, H. Oberlack, R. R. Ross, R. Barloutaud, P. Granet, J. Meyer, J. P. Porte, and J. Prevost, Nucl. Phys. **B21**, 15 (1970).

¹⁵D. Morgan, Phys. Rev. **166**, 1731 (1968); D. Morgan and G. Shaw, Phys. Rev. **D 2**, 520 (1970).

¹⁶B. Deler and G. Valladas, Nuovo Cimento **45A**, 559 (1966).

¹⁷Particle Data Group, Rev. Mod. Phys. **43**, S1 (1971). The decay asymmetry parameter is 0.645 ± 0.016 .

We have assumed the S- and P-wave amplitudes are relatively real; neglecting the small relative phase of $-6.3^\circ \pm 3.5^\circ$.

¹⁸Philippe H. Eberhard and Werner O. Koellner, Lawrence Radiation Laboratory Reports No. UCRL-20159, 1970 and No. UCRL-20160, 1971 (unpublished). The accuracy of the coding of the amplitudes and the relevant kinematics into the fitting program was checked in a variety of ways. The isobar-model amplitudes were calculated for a set of standard events and compared with the amplitudes calculated by other programs independently coded at Lawrence Berkeley Laboratory, Berkeley; SLAC, Stanford; and CEN, Saclay. In addition, Monte Carlo events were used to generate a variety of mass and angular distributions for each wave of Table III, and these were checked to be physically consistent with the quantum numbers. The polarization calculations were checked explicitly by hand for several events.

¹⁹Particle Data Group, Rev. Mod. Phys. **43**, S1 (1971).

²⁰The following masses were used to calculate the mixing angle: $m_N = 1515 \pm 15$, $m_\Sigma = 1670 \pm 10$, $m_\Lambda = 1690 \pm 10$,

$m_\Xi = 1832 \pm 37$, and $m_\Lambda = 1518 \pm 2$ MeV.

²¹R. Barloutaud (private communication).

²²The analysis of Ref. 5 uses an expression for this ratio which yields 3.3. We believe that the expression incorrectly normalizes the Breit-Wigner weight used to calculate an average $\Sigma(1385)$ momentum over the Dalitz plot. The normalization of this weight should be independent of the incident momentum. If this change is made, their expression yields a result consistent with ours.

²³See, for example, R. H. Dalitz, in *Symmetries and Quark Models*, edited by R. Chand (Gordon and Breach, New York, 1970).

²⁴David Faiman and Archibald Hendry, Phys. Rev. **173**, 1720 (1968); **180**, 1572 (1969); David Faiman, Nucl. Phys. **32B**, 573 (1971).

²⁵B. R. Martin and M. Sakitt, Phys. Rev. **183**, 1352 (1969).

K^+p and K^+d Total Cross Sections in the Momentum Range 0.57–1.16 GeV/c*

T. Bowen, E. W. Jenkins, R. M. Kalbach, D. V. Petersen,† and A. E. Pifer
Department of Physics, University of Arizona, Tucson, Arizona 85721

and

P. K. Caldwell‡
Department of Physics, University of Michigan, Ann Arbor, Michigan 48104
(Received 9 August 1972)

K^+p and K^+d total cross sections were measured in the momentum range 0.57–1.16 GeV/c using a secondary, separated kaon beam of the Lawrence Berkeley Laboratory Bevatron and conventional transmission-counter techniques. No evidence was found for structure in the cross section of either reaction as previously indicated near 0.7 GeV/c.

Previous experimental results^{1,2} have shown structure in both K^+p and K^+d total cross sections near 0.7-GeV/c incident momentum. Since this structure was observed near the upper limit of the momentum range which could be covered in our previous experiment,¹ it could not be investigated in great detail. The present experiment was designed to cover the momentum interval from 0.57 to 1.16 GeV/c so as to permit a systematic study of the region near 0.7 GeV/c as well as to provide for further detailed evidence on any other structure in this region.

The experiment was performed using a standard transmission-counter technique employing much of the apparatus of the previous experiment.¹ Although the beam was, as in the previous experiment, a separated kaon beam derived from a target in an external proton beam of the LBL Bevatron, the present beam transport system was designed to provide kaons of higher maximum mo-

mentum. Accordingly, principal differences from the previous experiment involve changes in the beam transport system and in the configuration of beam-defining counters appropriate for the higher momenta employed.

The beam could be tuned to momenta up to 1.5 GeV/c and consisted typically of 10^3 K^+ 's/pulse, along with 10^4 protons, 10^4 pions and muons, and 10^3 positrons. Figure 1 shows the bending and focusing magnets which comprise the beam transport system together with the beam-defining counters. Selection of kaons was accomplished with the use of three Čerenkov counters: one made of quartz, C_0 , one of Plexiglas, C_1 , and one threshold counter, C_2 , employing Freon gas at variable pressure. Additional selection was based on time-of-flight criteria using the two pairs of beam counters, S_1S_3 and S_2S_4 . This system gave a rejection ratio $>2 \times 10^4$ for particles other than kaons.

The target assembly consisted of three identical